SCIENCE CHINA Materials ARTICLES

mater.scichina.com link.springer.com

Published online 26 October 2020 | https://doi.org/10.1007/s40843-020-1470-5
Sci China Mater 2021, 64(3): 537–546

Band alignment towards high-efficiency NiO_x-based Sn-Pb mixed perovskite solar cells

Hao Chen[1,2,3†], Zijian Peng[1†], Kaimin Xu[1], Qi Wei[1], Danni Yu[1], Congcong Han[1], Hansheng Li[1] and Zhijun Ning[1*]

ABSTRACT **Narrow-bandgap tin-lead (Sn-Pb) mixed perovskite solar cells (PSCs) play a key role in constructing perovskite tandem solar cells that are potential to overpass Shockley-Queisser limit. A robust, chemically stable and low-temperature-processed hole transporting layer (HTL) is essential for building high-efficiency Sn-Pb solar cells and perovskite tandem solar cells. Here, we explore a room-temperature-processed NiO_x (L-NiO_x) HTL based on nanocrystals (NCs) for Sn-Pb PSCs. In comparison with high-temperature-annealed NiO_x (H-NiO_x) film, the L-NiO_x film shows deeper valence band and lower trap density, which increases the built-in potential and reduces carrier recombination, leading to a power conversion efficiency of 18.77%, the record for NiO_x-based narrow-bandgap PSCs. Furthermore, the device maintains about 96% of its original efficiency after 50 days. This work provides a robust and room-temperature-processed HTL for highly efficient and stable narrow-bandgap PSCs.**

Keywords: band alignment, NiO_x, Sn-Pb mixed perovskite, solar cell

INTRODUCTION

Narrow-bandgap (~1.25 eV) tin-lead (Sn-Pb) mixed perovskite solar cells (PSCs) have aroused great interest for their broad absorption in infrared region and lower toxicity in comparison with lead PSCs. Recently, based on the combination of wide-bandgap PSCs and narrow-bandgap Sn-Pb PSCs, 2-terminal perovskite-perovskite tandem solar cell shows a power conversion efficiency (PCE) of 24.8% [1].

Currently, most high-efficiency Sn-Pb mixed PSCs are based on organic hole transporting layer (HTL) such as poly (3,4-ethylenedioxythiophene)-poly(styrenesulfonate) (PEDOT:PSS) [2–7]. For example, Yan, Zhu and co-workers [8] recently increased the PCE of Sn-Pb mixed PSCs up to 20% by using PEDOT:PSS as HTL. However, due to its strong acidity and hydrophilicity, PEDOT:PSS is potential to induce the degradation of the devices [9–11]. It is therefore highly desirable to develop stable HTL for high-efficiency narrow-bandgap PSCs.

Inorganic semiconductors, such as NiO_x, CuI, CuSCN, Cu_2O, and MoO_3 are reported as HTLs for PSCs [9,12–23]. Among all kinds of inorganic HTL materials, NiO_x is widely used in PSCs due to its intrinsic p-type doping characteristic, excellent chemical stability and high optical transmittance. Recently, using solution-processed NiO_x nanoparticles as HTL, Pb PSCs exhibit PCE close to 22% [24]. However, Sn-Pb mixed PSCs based on NiO_x thin films generally show low efficiency [25–27]. One imprtant reason is the band structure misalignment between NiO_x and the perovskite film. Furthermore, for Sn-Pb mixed devices, NiO_x HTL is generally fabricated *via the* high-temperature annealing process, which is incompatible for the fabrication of flexible and tandem solar cells.

In this study, we explore a room-temperature-prepared NiO_x (L-NiO_x) nanocrystal (NC) film as HTL for Sn-Pb PSCs. In comparison with conventional NiO_x by high-temperature annealing (H-NiO_x), the L-NiO_x HTL shows deeper work function bringing higher built-in potential. As a result, the Sn-Pb PSCs demonstrate a PCE up to 18.77%, which, to the best of our knowledge, is the

[1] School of Physical Science and Technology, ShanghaiTech University, Shanghai 201210, China
[2] Shanghai Institute of Ceramics, Chinese Academy of Sciences, Shanghai 200050, China
[3] School of Chemistry and Chemical Engineering, University of Chinese Academy of Sciences, Beijing 100049, China
† These authors contributed equally to this work.
* Corresponding author (email: ningzhj@shanghaitech.edu.cn)

highest efficiency reported among the NiO_x-based narrow-bandgap PSCs.

EXPERIMENTAL SECTION

Materials

Lead iodide (PbI_2) and bathocuproine (BCP) were purchased from TCI. Anhydrous dimethylsulfoxide (DMSO), anhydrous dimethylformamide (DMF), anhydrous isopropyl alcohol (IPA), chlorobenzene (CB), $Pb(SCN)_2$, and SnF_2 were purchased from Sigma-Aldrich. Methylammonium iodide (MAI) was purchased from Shanghai MaterWin New Materials Technology Co., Ltd. Formamidinium iodide (FAI) was purchased from Xi'an Polymer Light Technology Cory. All salts and solvents were used as received without any further purification.

Density function theory calculation for electronic structure of NiO_x

All the calculations here were performed by using the Vienna *ab-initio* Simulation Package (VASP) code in the framework of density function theory (DFT) [28,29]. The electron-ion interaction was described by the projector augmented wave (PAW) method [30]. The generalized gradient approximation (GGA) of Perdew-Burke-Ernzerhof (PBE) was used for the exchange-correlation functional [31]. The plane-wave cutoff energy was set to 400 eV. The Gamma-centered k-point mesh with grid spacing of $2\pi \times 0.02$ Å^{-1} was used for electronic Brillouin zone integration. Because of strong electronic correlations between 3d electrons of NiO, electronic correlations were also included in a simple rotationally invariant DFT+U version [32]. Following previous work [33], the optimal combination of Hubbard parameters (U = 6.3 eV and J = 1 eV) were used to improve the prediction of the electronic structure and magnetic properties. And present GGA+U calculations predict the AFII (stacking of ferromagnetic planes in [111] direction of rocksalt structure) as the most stable magnetic configuration of NiO. A 5×5×2 supercell was constructed to represent the NiO with 1.3% nickel vacancy. To remain the antiferromagnetic property, two nickel atoms with opposite magnetic moment were removed from the supercell.

Syntheses of NiO_x NCs

The NiO_x NCs were prepared *via* the hydrolysis reaction of nickel nitrate referring to our previous work [24]. Briefly, 20 mmol $Ni(NO_3)_2{\cdot}6H_2O$ was dissolved in 20 mL of deionized water to obtain a dark green solution. Then, 4 mL of NaOH aqueous solution (10 mol L^{-1}) was slowly added into the solution while stirring. After being stirred for 20 min, the colloidal precipitation was thoroughly washed with deionized water three times and dried at 80°C for 6 h. The obtained green powder was then calcined at 270°C for 2 h to obtain a dark-black powder.

H-NiO_x precursor solution preparation

$Ni(NO_3)_2{\cdot}6H_2O$ (279.79 mg) was dissolved in 2-methoxyethanol (10 mL). After the solution was stirred at 50°C for 1 h, 100 μL acetylacetone was added to the solution, and then the solution was further stirred overnight at room temperature.

Sn-Pb perovskite precursor preparation

$(FASnI_3)_{0.6}(MAPbI_3)_{0.4}$ (FAMA) perovskite precursor was prepared as reported with some modification [2]. The $FASnI_3$ precursor solution was prepared by dissolving 428.4 mg of SnI_2 and 197.8 mg of FAI with 10 mol% (18 mg) of SnF_2 in 800 μL DMF and 200 μL DMSO, with stirring at room temperature. The $MAPbI_3$ precursor solution was prepared by dissolving 530 mg PbI_2 and 183 mg MAI with 3.5 mol% (13.2 mg) lead thiocyanate ($Pb(SCN)_2$) dissolved in 630 μL DMF and 70 μL DMSO, with stirring at 70°C for 30 min. The FAMA precursor solution was obtained by mixing stoichiometric amounts of $FASnI_3$ (0.6 mL) and $MAPbI_3$ (0.4 mL) perovskite precursor and stirring at room temperature for 30 min.

Fabrication of Sn-Pb perovskite solar cells

The pre-patterned indium tin oxide (ITO) substrates were cleaned by ultrasonication in deionized water bath with 2% Triton X-100, deionized water and isopropanol for 30 min each, respectively. Before using, the ITO substrates were cleaned by ultraviolet ozone (UVO) treatment for 20 min. L-NiO_x films were fabricated by spin-coating NiO_x NC ink on the cleaned ITO substrate at 2000 r min^{-1} for 40 s (at room temperature) without any post-treatment. H-NiO_x films were deposited by spin-coating the H-NiO_x precursor solution at 5000 r min^{-1} for 45 s and annealed at 250°C for 45 min. PEDOT:PSS films were coated on the cleaned ITO substrate at 4000 r min^{-1} for 50 s and then dried at 175°C for 30 min. The FAMA perovskite precursors were spin-coated onto the substrate at 4000 r min^{-1} for 60 s, and 500 mL toluene was dropped on the spinning substrate during the spin-coating step 45 s before the end of the procedure. All perovskite films were annealed at 40°C for 1 min and then at 70°C for 10 min on a hotplate. Next, 20 mg mL^{-1} [6,6]-phenyl-C_{61}-butyric acid methyl ester (PCBM) in chlorobenzene was spin coated at 1500 r min^{-1} for 50 s and then annealed at

70°C for 5 min. Then, a thin and uniform BCP layer on top of PCBM was deposited by drop-casting a defined volume of BCP dissolved in isopropyl alcohol in 2 to 3 s while spinning the substrate at 5000 r min^{-1}. Finally, 120 nm Ag contact was deposited on top of BCP by thermal evaporation under high vacuum (< 5×10^{-7} Torr) in an Angstrom Engineering deposition system. All fabrication steps of perovskite films and top layers were performed in an N_2-purged glovebox (Vigor Glovebox, O_2 < 0.1 ppm, H_2O < 0.1 ppm).

Characterizations

The X-ray diffraction (XRD) spectra were measured on a Bruker D8 Advance X-ray diffractometer at room temperature using Cu-Kα radiation (λ = 1.54178 Å) at 40 kV and 40 mA. The photoluminescence (PL) spectra were carried out using an exciting wavelength of 400 nm with a Fluorolog spectrofluorometer (Horiba FL-3) with a standard 450 W xenon CW lamp. The ultraviolet-visible (UV-Vis) spectra of the perovskite films deposited on NiO_x were recorded using a UV-Vis spectrophotometer (Agilent Cary 5000). Scanning electron microscopy (SEM) images were recorded on JSM-7800. The current-voltage (*J-V*) characteristics of the photovoltaic cells were obtained using a Keithley 2400 Source Meter under simulated one-sun AM 1.5 G illumination (100 mW cm^{-2}) with a solar simulator (SS-F5-3A, Enli Tech) whose intensity was calibrated by the certified standard silicon solar cell (SRC-2020, Enli Tech). The *J-V* curves for all devices were measured by masking the active area using a metal mask with an area of 0.04 cm^2. The external quantum efficiency (EQE) was measured using the solar-cell-spectra-response measurement system (QE-R, Enli Tech). The Mott-Schottky analysis through capacitance-voltage measurements was collected by Ivium electrochemical workstation at 1 kHz with the bias potentials ranging from 0 to 1 V under dark condition. The electrochemical impedance spectroscopy (EIS) analysis was performed on the Ivium electrochemical workstation at a bias close to open circuit voltage (V_{oc}) under dark condition with the frequency ranging from 1,000,000 to 1.0 Hz and amplitude (V) of 0.02.

RESULTS AND DISCUSSION

We first investigated the structures and morphologies of L-NiO_x and H-NiO_x. The crystallinities and sizes of NiO_x NCs were invrstigated by XRD and transmission electron microscopy (TEM). The L-NiO_x NC powder exhibits good crystallinity, as indicated from the XRD spectrum (Fig. 1a). TEM images indicate narrow size distribution

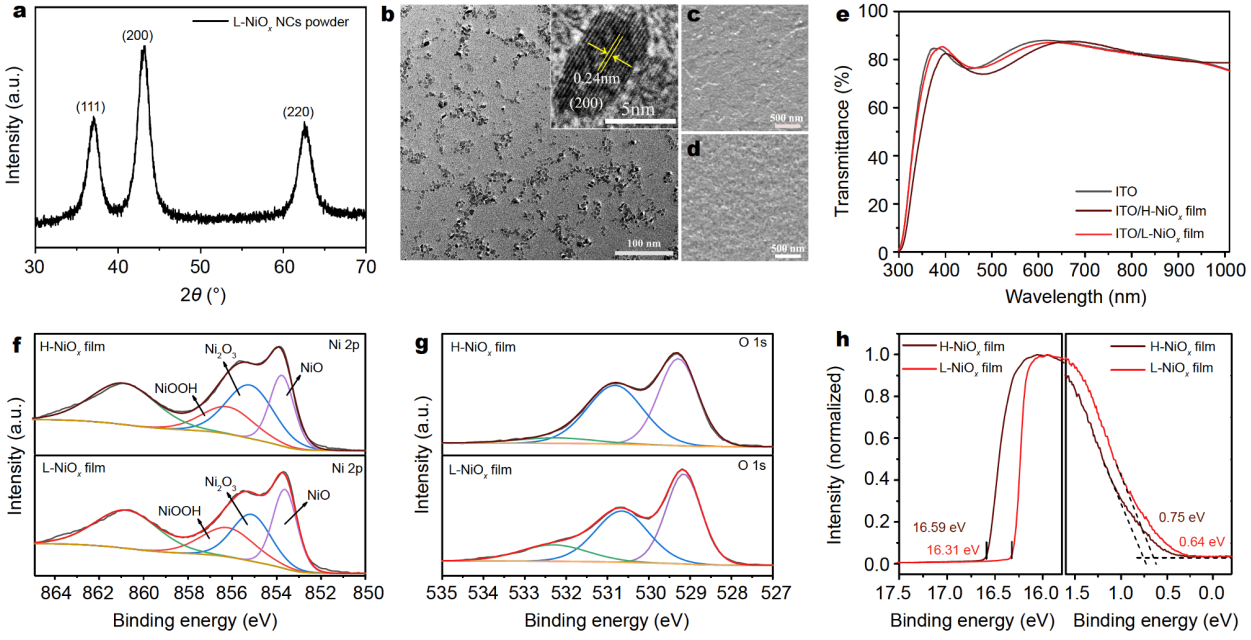

Figure 1 Characterizations of the NiO_x HTL. (a) XRD spectra of L-NiO_x NC powder. (b) TEM image of L-NiO_x NCs with an inset of the high-resolution TEM image of L-NiO_x NCs. (c, d) Top-view SEM images of H-NiO_x and L-NiO_x films deposited on ITO-coated glass. (e) Transmission spectra of ITO-coated glass, H-NiO_x and L-NiO_x films deposited on ITO-coated glass. (f) XPS spectra: Ni $2p_{3/2}$ of H-NiO_x and L-NiO_x films deposited on ITO-coated glass. (g) XPS spectra: O 1s of H-NiO_x and L-NiO_x films deposited on ITO-coated glass. (h) UPS characterization for H-NiO_x and L-NiO_x films deposited on ITO-coated glass. Left: photoemission cutoff spectra; right: valence band structure.

(with the size of about 5 nm) of NiO_x NCs (Fig. 1b). The morphology of NiO_x films was investigated by SEM and atomic force microscopy (AFM) (Fig. 1c, d, and Fig. S1). The L-NiO_x film is more compact and smooth in comparison with the H-NiO_x film. The absorption spectrum of L-NiO_x film is quite similar to that of ITO glass, and no extra absorption peak is observed in the range from 350 to 1000 nm (Fig. 1e). In contrast, a new absorption peak at 550 nm is observed for H-NiO_x film, which might be ascribed to the defects in the bandgap as discussed below.

The element compositions of resulting NiO_x thin films were analyzed by X-ray photoelectron spectroscopy (XPS). As shown in Fig. 1f, the Ni 2p peaks are derived from two states, Ni^{2+} state in NiO (Ni 2p at 853.8 eV), Ni^{3+} in Ni_2O_3 (Ni 2p at 855.2 eV) and NiOOH (Ni 2p at 856.2 eV). Similarly, O 1s shows three peaks from NiO (529.2 eV), Ni_2O_3 (530.8 eV), and hydroxide (532.3 eV), respectively (Fig. 1g). Compared with the H-NiO_x film, the L-NiO_x film has a lower ratio of Ni^{3+}/Ni^{2+}, indicating the L-NiO_x film has reduced nickel vacancy.

We then investigated the band structure of NiO_x films *via* ultraviolet photoelectron spectroscopy (UPS). As shown in Fig. 1h, the work function (W_F) of the H-NiO_x and L-NiO_x films are 4.63 and 4.91 eV, respectively. Based on the binding energy values, the energy levels of the valence band maximum are calculated to be 5.38 and 5.55 eV for the H-NiO_x and L-NiO_x films, respectively. The better energy level alignment between L-NiO_x and Sn-Pb perovskite contributes to the hole extraction from perovskite to HTL.

DFT simulation was used to study the electronic structure of two kinds of NiO_x materials, pure NiO and NiO with 1.3% Ni vacancy ($Ni_{148}O_{150}$), representing L-NiO_x and H-NiO_x, respectively (Fig. 2). The calculated bandgap and magnetic moment for pure NiO are 3.12 eV and 1.70 μB, respectively, close to the real value [34]. The simulation indicates that Ni vacancies in bulk NiO induce the gap states and result in shallower valence band. This is consistent with the UPS results above.

XRD patterns of the perovskite films prepared on NiO_x substrates are shown in Fig. 3a. The FAMA film grown on the L-NiO_x film shows strong diffraction peaks from (110) and (220) facets, indicating a pure phase and high crystallinity of perovskite layer. The element compositions of the resulting Sn-Pb perovskite film based on L-NiO_x were analyzed by XPS (Fig. S2). The atomic percentages of Sn and Pb are 8.53% and 5.76% (Table S1), respectively, corresponding to an atomic ratio of 6:4,

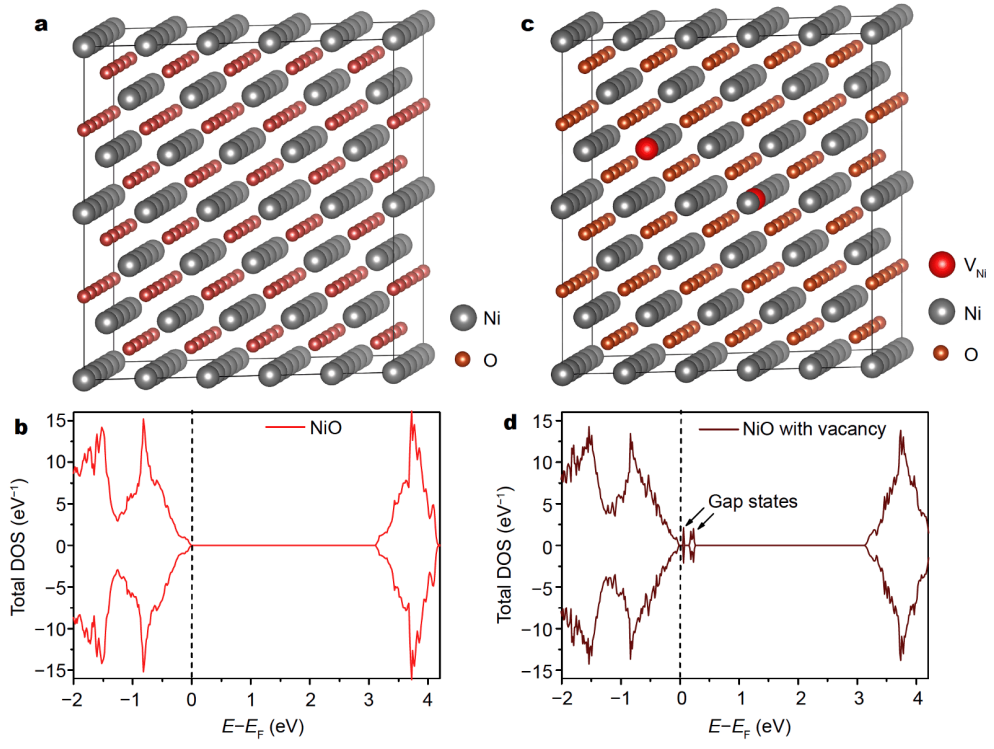

Figure 2 (a) Atomic model and (b) the total DOS of NiO, (c) atomic model and (d) the total DOS of NiO with Ni vacancy. The corresponding gap states are labeled with arrows.

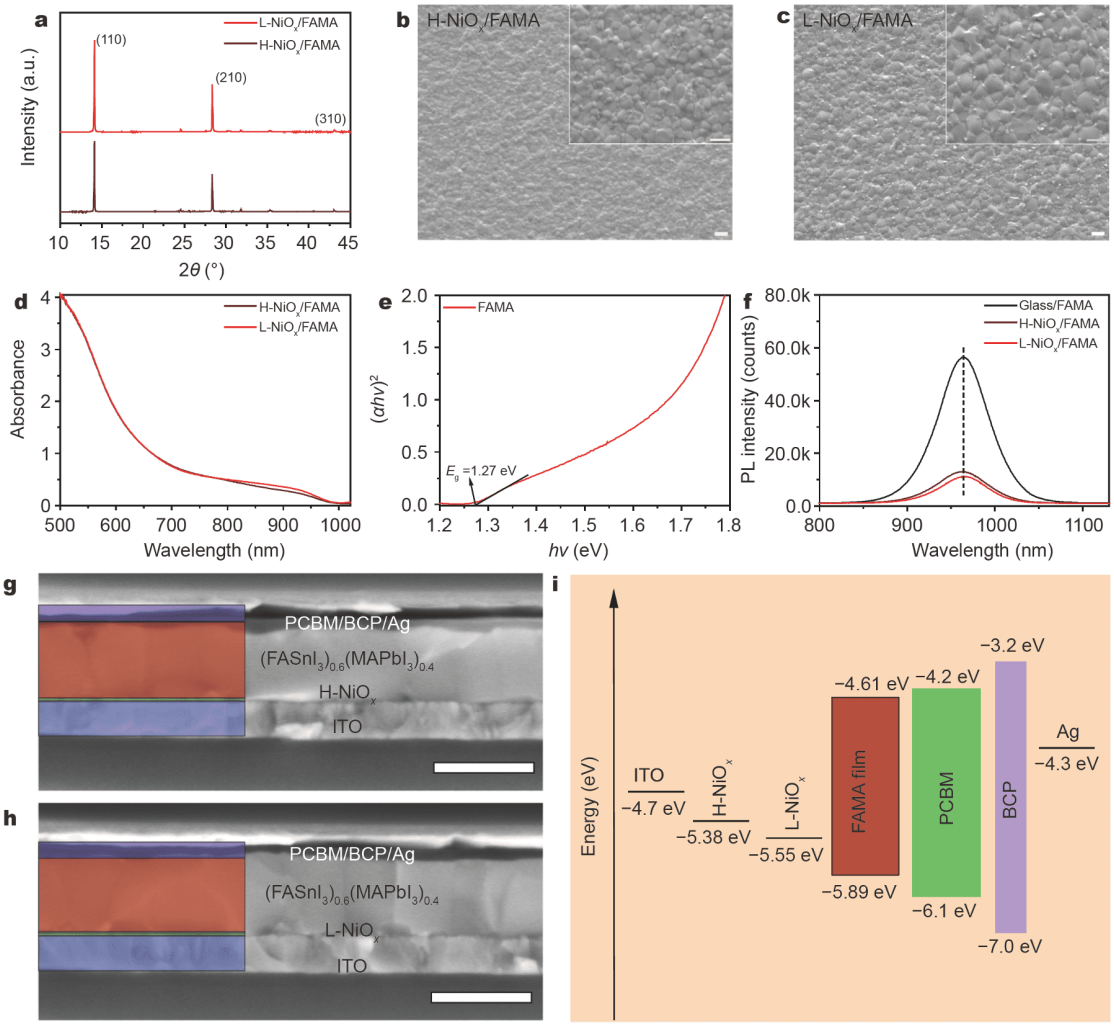

Figure 3 Characterizations of FAMA films grown on H-NiO_x and L-NiO_x films. (a) XRD patterns of FAMA films. (b, c) Top-view SEM images of FAMA films (Scale bar: 500 nm). (d) UV-Vis absorption spectra of FAMA films. (e) Tauc plot of FAMA films. (f) PL spectra of FAMA films. (g, h) Cross-sectional SEM images of devices (scale bar: 500 nm). (i) Energy-level diagram with respect to vacuum of the materials used in the photovoltaic cells.

which agrees well with that of the starting precursor. UPS was used to analyze the electronic structure of the perovksite film (Fig. S3), and the energy level of valence band maximum of Sn-Pb perovskite is determined to be 5.89 eV.

The SEM images of the FAMA perovskite films on NiO_x substrates are shown in Fig. 3b, c. Both samples show compact and pin-hole free morphology, but the film deposited on L-NiO_x exhibits larger crystal, which agrees well with the XRD result. The smaller grain size of the perovskite film based on H-NiO_x could be ascribed to its high defect density and large surface roughness, which increased the concentration of nucleation centers [35–38].

The absorption spectra of FAMA perovskite films deposited on NiO_x substrates are shown in Fig. 3d. The bandgap of FAMA sample is determined to be about 1.27 eV by fitting the absorption plot of a perovskite film (Fig. 3e). The film deposited on glass exhibits the highest PL intensity with the peak emission centered around 964 nm (Fig. 3f). The films coated on L-NiO_x and H-NiO_x films both show lower PL intensity due to the hole transfer from the perovskite to NiO_x HTLs. The time-resolved PL decay spectra of FAMA films deposited on NiO_x are shown in Fig. S4. The faster decay of L-NiO_x/FAMA indicates that the L-NiO_x film has higher charge extraction efficiency. We carried out XPS characterization to study the impact of the Ni^{3+} from NiO_x substrates to

Sn^{2+} oxidation of Sn-Pb perovskite film (Figs S5 and S6). Sn^{4+} peak is not observed at the interface for both fresh and aged films, which means Ni^{3+} would not oxidize Sn^{2+} to Sn^{4+} in the samples. The retardance of oxidation could be ascribed to the kinetic barrier at the interface, although this reaction is thermodynamically favorable.

We fabricated the Sn-Pb PSCs using the p-i-n structure of ITO/HTL/FAMA/PCBM/BCP/Ag. The schematic of the Sn-Pb devices and the processing temperatures of each layer are illustrated in Fig. S7. The whole devices were made under the temperature below 70°C. The cross-sectional SEM images of the devices show that the thickness of the absorber layer is about 400 nm (Fig. 3g, h). The performance of the devices based on NiO_x HTL are shown in Fig. 4a. The champion device based on L-NiO_x exhibits a V_{oc} of 0.82 V, short circuit current (J_{sc}) of 29.6 mA cm^{-2}, fill factor (FF) of 77.2% and PCE of 18.77%. While the device using H-NiO_x demonstrates a V_{oc} of 0.78 V, J_{sc} of 28.3 mA cm^{-2}, FF of 71.6%, and PCE of 15.85%. Both NiO_x-based devices exhibit negligible hysteresis (Fig. 4b and Fig. S8). The *J-V* curves of the devices based on L-NiO_x of different thicknesses by using different concentrations of L-NiO_x solution are shown in Fig. S9, which indicates that 10 mg mL^{-1} is the optimal

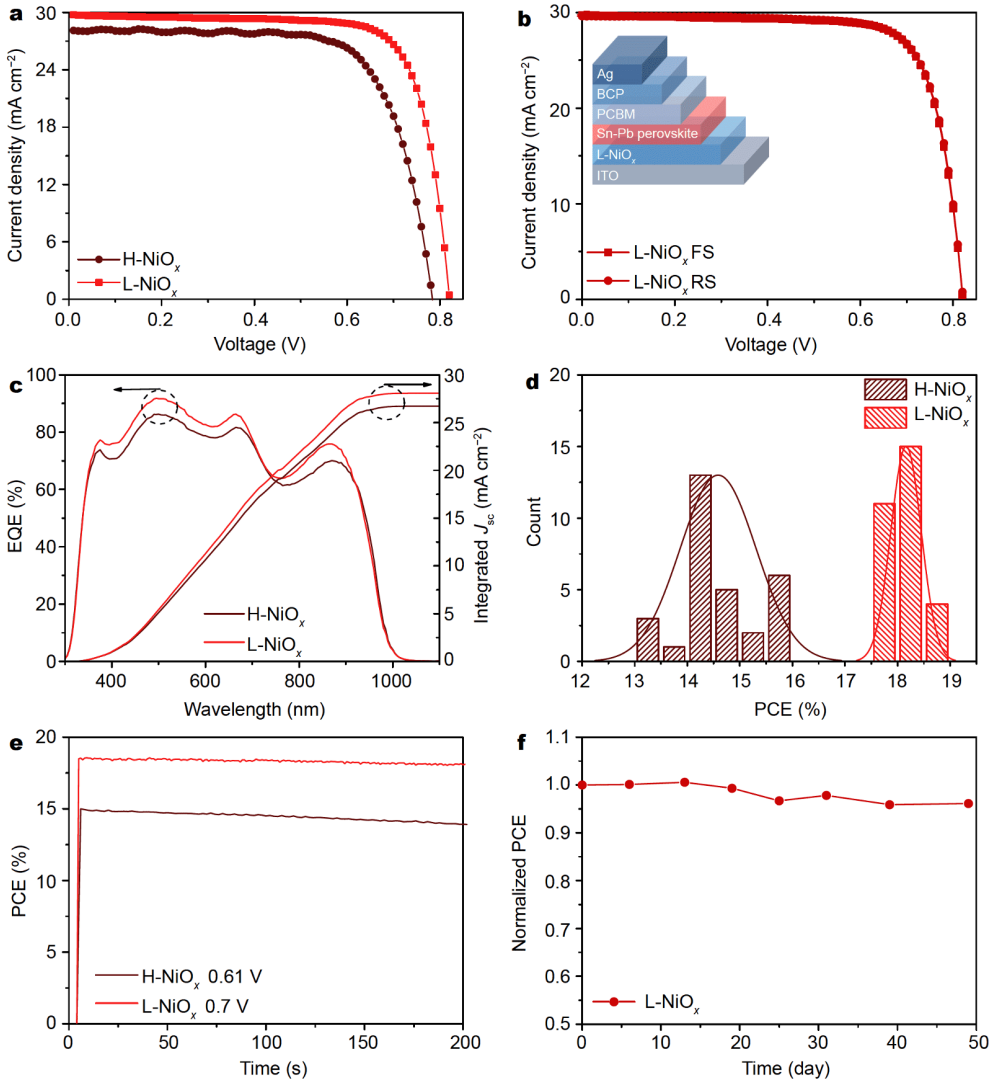

Figure 4 (a) *J-V* characteristics from forward scan (FS, J_{sc} to V_{oc}) of the devices determined under simulated AM 1.5 G illumination. (b) *J-V* characteristics from FS (J_{sc} to V_{oc}) and reverse scan (RS, V_{oc} to J_{sc}) determined under simulated AM 1.5 G illumination for champion L-NiO_x-based device. The inset shows the device structure. (c) The corresponding incident photon-to-electron conversion efficiency (IPCE) spectra of the devices. (d) Histogram of the PCE values for the devices. (e) Stabilized PCEs of the devices measured at a bias of V_{max} under 100 mW cm^{-2} AM 1.5 G irradiation. (f) Stability of Sn-Pb devices under N_2 atmosphere.

concentration for L-NiO_x film fabricatation. A control device based on PEDOT:PSS was prepared as well, showing an efficiency of 17% (Table S2 and Fig. S10). The devices based on the L-NiO_x film deliver evidently higher V_{oc}, as well as higher J_{sc}. The EQE curves of the devices are presented in Fig. 4c. The devices exhibit a broad response spectrum in the range of 300 to 980 nm. The values of integrated J_{sc} are 28.1 and 26.7 mA cm^{-2} for L-NiO_x-based and H-NiO_x-based devices, respectively, which agree well with the values extracted from the *J-V* curves.

For each kind of device, we fabricated 30 devices to get statistics about the performance. The average PCEs of the devices based on L-NiO_x and H-NiO_x are 18.18% and 14.64%, respectively (Fig. 4d and Table 1). To estimate the stability of the device under operation, the steady state PCEs were measured. The steady-state PCE of L-NiO_x-based device at a constant bias of 0.70 V is 18.4%, well consistent with the efficiency extracted from the *J-V* curve. We summarized the PCEs of Sn-Pb PSCs using NiO_x-based inverted structures (Table S3). To the best of our knowledge, the value of 18.4% is the highest efficiency reported up to now.

The stabilities of the Sn-Pb PSCs without encapsulation were investigated in nitrogen atmosphere. As shown in Fig. 4f, the stability of Sn-Pb PSCs based on the L-NiO_x film shows good stability: it maintains 96% of the initial PCE after 50 days. This great stability of the device could be due to the high-quality perovskite film and lower defect density at the interface, which suppresses the self-oxidation of Sn^{2+}.

To understand the high performance of the device based on L-NiO_x, we characterized the carrier recombination, carrier lifetime and dark current of the device. The carrier recombination was tested *via* light-dependent V_{oc}. H-NiO_x-based device exhibits a slope (V_{oc} with respect to natural logarithmic light intensity) of 1.62 kT q^{-1}. By contrast, for the L-NiO_x-based device, the slope decreases to 1.44 kT q^{-1}, showing reduced trap-assisted recombination (Fig. 5a) [39,40]. The transient photovoltage measurement was carried out to study the carrier lifetime, as shown in Fig. 5b. The carrier lifetime of L-NiO_x-based device increases to 65.8 μs compared with H-NiO_x-based devices (9.1 μs), indicating the reduced carrier recombination at the interface between L-NiO_x and perovskite film [41–43]. We then compared the dark *J-V* curves of the devices (Fig. 5c). The lower reverse saturation current density indicates that the L-NiO_x-based devices posses better diode behavior and less charge recombination [26], most probably deriving from the low defect density of the L-NiO_x film.

The capacitance-voltage (*C-V*) characteristics of the Sn-Pb devices were taken to understand the V_{oc} improvement. As shown in Fig. 5d, the L-NiO_x-based device has a higher built-in potential (V_{bi}) of 0.56 V compared with the H-NiO_x-based device (0.52 V). The increased V_{bi} can be attributed to the higher work function of the L-NiO_x film.

To quantify the reduced trap-state density at the interface of perovskite films and HTL, we calculated the trap density (n_t) by space-charge-limited current (SCLC) measurement in the hole-only devices. The trap-state density n_t can be calculated by the following relation:

$$n_t = \frac{V_{TFL} \times \varepsilon \times \varepsilon_0}{e \times L^2},$$

where e is the elementary charge, L is the perovskite film thickness, ε_0 is the vacuum permittivity, ε is the relative dielectric constant (typically 35 for perovskites), and V_{TFL} is the onset voltage of trap-filled limit (TFL) region. As shown in Fig. 5e, The V_{TFL} of H-NiO_x-based device is 0.45 V, corresponding to a trap-state density of 5.45×10^{15} cm^{-3}. Upon using L-NiO_x as HTL, the V_{TFL} is reduced to 0.22 V, and the calculated hole trap-state density is 2.66×10^{15} cm^{-3}. This result confirms that the L-NiO_x-based Sn-Pb device reduced the hole trap-state density at the interface of perovskite layers.

We further used EIS to understand the charge extraction and recombination processes of the devices, as shown in Fig. 5f. The fitted equivalent circuit of the devices is composed of series resistance (R_s), charge transfer resistance (R_{tr}) at interfaces, and recombination resistance (R_{rec}) inside the perovskite film (Fig. S11) [3,44–46]. The larger arc of L-NiO_x NCs-based PSCs suggests a slower charge recombination rate as well, which can be ascribed to the less trap-state density at the interfaces. Fig. S12 shows the transient photocurrent change as light illumination itensity. The high α value (0.98) close to unity of

Table 1 Photovoltaic parameters of PSCs with different HTLs

HTL	V_{oc} (V)	J_{sc} (mA cm^{-2})	FF (%)	PCE (%)
H-NiO_x	0.78 ± 0.01 (0.80)	27.6 ± 0.6 (28.5)	68.0 ± 3.0 (72.5)	14.64 ± 0.67 (15.85)
L-NiO_x	0.83 ± 0.01 (0.84)	28.8 ± 0.5 (29.6)	76.1 ± 0.9 (77.4)	18.18 ± 0.30 (18.77)

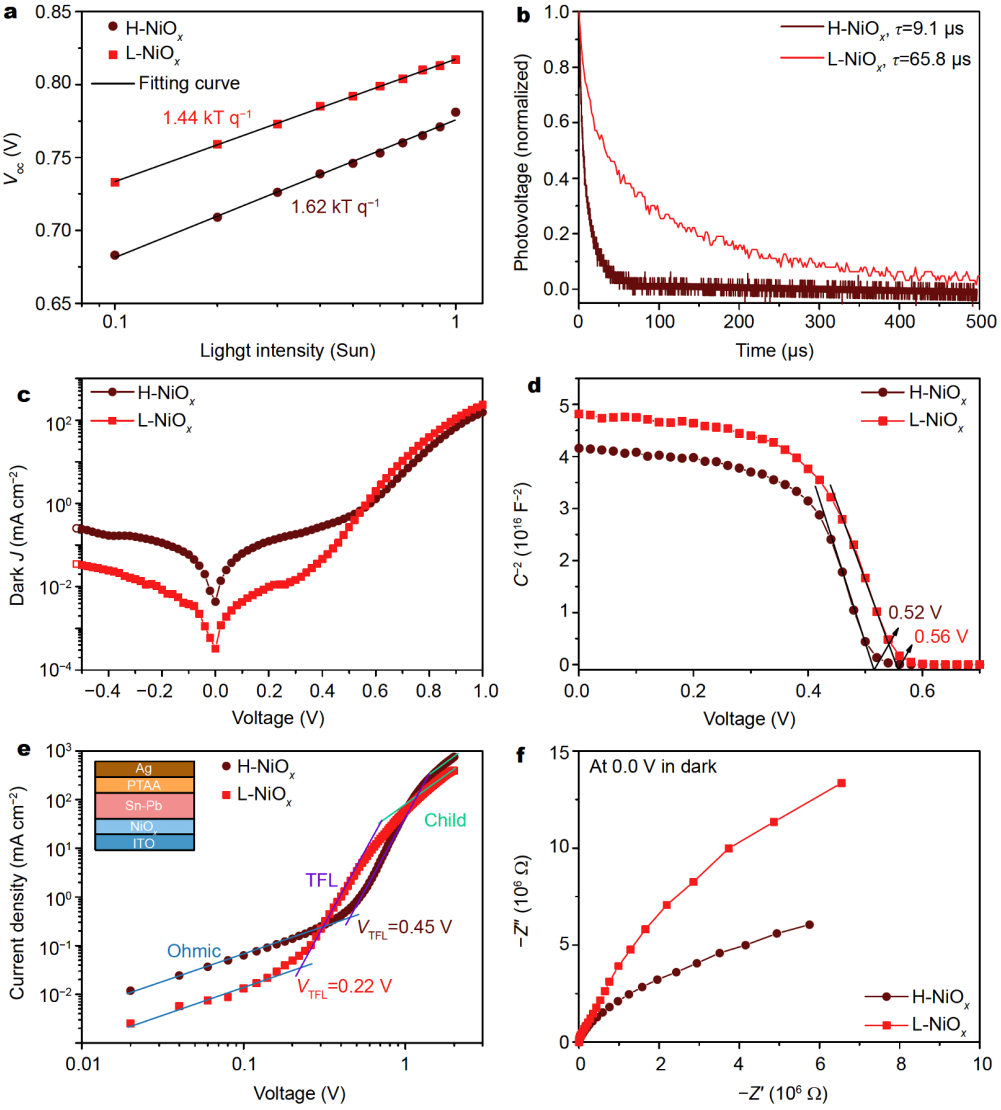

Figure 5 Electronic properties of the devices based on H-NiO_x and L-NiO_x films. (a) V_{oc} dependence upon light intensity of devices. (b) Transient photovoltage measurements of solar cells. (c) Dark *J*-*V* curves for PSCs. (d) *C*-*V* measurements of PSCs. (e) SCLC measurement for trap-state density based on the hole-only devices (the structure is shown in the inset). (f) Nyquist plot under dark of devices at short circuit condition.

the NiO_x NCs-based device indicates that almost all free carriers are swept out and collected at the electrodes prior to bimolecular recombination.

CONCLUSION

In conclusion, we report a room-temperature-processed NiO_x film as HTL for planar structural Sn-Pb mixed PSCs. In comparison with H-NiO_x, L-NiO_x shows reduced trap density and deeper energy level. Solar cells based on L-NiO_x display much reduced carrier recombination and higher built-in potential; as a result, the device based on L-NiO_x exhibits enhanced V_{oc} and J_{sc}. The device demonstrates an unprecedently high efficiency of 18.77% for low-temperature-processed narrow-bandgap PSCs. Moreover, the optimized device shows impressive stability. This work provides an effective strategy to build low-temperature-processed narrow-bandgap PSCs, which could be useful for constructing high-efficiency tandem solar cells.

Received 28 March 2020; accepted 23 July 2020; published online 26 October 2020

1 Lin R, Xiao K, Qin Z, *et al.* Monolithic all-perovskite tandem solar cells with 24.8% efficiency exploiting comproportionation to sup-

press Sn(II) oxidation in precursor ink. Nat Energy, 2019, 4: 864–873
2 Kapil G, Ripolles TS, Hamada K, *et al.* Highly efficient 17.6% tin-lead mixed perovskite solar cells realized through spike structure. Nano Lett, 2018, 18: 3600–3607
3 Xu G, Bi P, Wang S, *et al.* Integrating ultrathin bulk-heterojunction organic semiconductor intermediary for high-performance low-bandgap perovskite solar cells with low energy loss. Adv Funct Mater, 2018, 28: 1804427
4 Zhu Z, Li N, Zhao D, *et al.* Improved efficiency and stability of Pb/Sn binary perovskite solar cells fabricated by galvanic displacement reaction. Adv Energy Mater, 2019, 9: 1802774
5 Pargoletti E, Hossain UH, Di Bernardo I, *et al.* Room-temperature photodetectors and VOC sensors based on graphene oxide-ZnO nano-heterojunctions. Nanoscale, 2019, 11: 22932–22945
6 Wei M, Xiao K, Walters G, *et al.* Combining efficiency and stability in mixed tin-lead perovskite solar cells by capping grains with an ultrathin 2D layer. Adv Mater, 2020, 32: 1907058
7 Gu S, Lin R, Han Q, *et al.* Tin and mixed lead-tin halide perovskite solar cells: Progress and their application in tandem solar cells. Adv Mater, 2020, 1907392
8 Tong J, Song Z, Kim DH, *et al.* Carrier lifetimes of >1 μs in Sn-Pb perovskites enable efficient all-perovskite tandem solar cells. Science, 2019, 364: 475–479
9 You J, Meng L, Song TB, *et al.* Improved air stability of perovskite solar cells *via* solution-processed metal oxide transport layers. Nat Nanotech, 2016, 11: 75–81
10 Liu Z, Chang J, Lin Z, *et al.* High-performance planar perovskite solar cells using low temperature, solution-combustion-based nickel oxide hole transporting layer with efficiency exceeding 20%. Adv Energy Mater, 2018, 8: 1703432
11 Ye L, Fan B, Zhang S, *et al.* Perovskite-polymer hybrid solar cells with near-infrared external quantum efficiency over 40%. Sci China Mater, 2015, 58: 953–960
12 Park JH, Seo J, Park S, *et al.* Efficient $CH_3NH_3PbI_3$ perovskite solar cells employing nanostructured p-type NiO electrode formed by a pulsed laser deposition. Adv Mater, 2015, 27: 4013–4019
13 Wang H, Yu Z, Jiang X, *et al.* Efficient and stable inverted planar perovskite solar cells employing CuI as hole-transporting layer prepared by solid-gas transformation. Energy Technol, 2017, 5: 1836–1843
14 Ye S, Sun W, Li Y, *et al.* CuSCN-based inverted planar perovskite solar cell with an average PCE of 15.6%. Nano Lett, 2015, 15: 3723–3728
15 Zuo C, Ding L. Solution-processed Cu_2O and CuO as hole transport materials for efficient perovskite solar cells. Small, 2015, 11: 5528–5532
16 Schulz P, Tiepelt JO, Christians JA, *et al.* High-work-function molybdenum oxide hole extraction contacts in hybrid organic-inorganic perovskite solar cells. ACS Appl Mater Interfaces, 2016, 8: 31491–31499
17 Zhao K, Munir R, Yan B, *et al.* Solution-processed inorganic copper(i) thiocyanate (CuSCN) hole transporting layers for efficient p-i-n perovskite solar cells. J Mater Chem A, 2015, 3: 20554–20559
18 Arora N, Dar MI, Hinderhofer A, *et al.* Perovskite solar cells with CuSCN hole extraction layers yield stabilized efficiencies greater than 20%. Science, 2017, 358: 768–771
19 Chatterjee S, Pal AJ. Introducing Cu_2O thin films as a hole-transport layer in efficient planar perovskite solar cell structures. J Phys Chem C, 2016, 120: 1428–1437
20 Yu W, Li F, Wang H, *et al.* Ultrathin Cu_2O as an efficient inorganic hole transporting material for perovskite solar cells. Nanoscale, 2016, 8: 6173–6179
21 Cao J, Wu B, Peng J, *et al.* Copper-copper iodide hybrid nanostructure as hole transport material for efficient and stable inverted perovskite solar cells. Sci China Chem, 2019, 62: 363–369
22 Qin P, He Q, Ouyang D, *et al.* Transition metal oxides as hole-transporting materials in organic semiconductor and hybrid perovskite based solar cells. Sci China Chem, 2017, 60: 472–489
23 Yu D, Hu Y, Shi J, *et al.* Stability improvement under high efficiency—Next stage development of perovskite solar cells. Sci China Chem, 2019, 62: 684–707
24 Chen H, Wei Q, Saidaminov MI, *et al.* Efficient and stable inverted perovskite solar cells incorporating secondary amines. Adv Mater, 2019, 31: 1903559
25 Yang Z, Rajagopal A, Chueh CC, *et al.* Stable low-bandgap Pb-Sn binary perovskites for tandem solar cells. Adv Mater, 2016, 28: 8990–8997
26 Chi D, Huang S, Zhang M, *et al.* Composition and interface engineering for efficient and thermally stable Pb-Sn mixed low-bandgap perovskite solar cells. Adv Funct Mater, 2018, 28: 1804603
27 Han Q, Wei Y, Lin R, *et al.* Low-temperature processed inorganic hole transport layer for efficient and stable mixed Pb-Sn low-bandgap perovskite solar cells. Sci Bull, 2019, 64: 1399–1401
28 Kresse G, Furthmüller J. Efficient iterative schemes for *ab initio* total-energy calculations using a plane-wave basis set. Phys Rev B, 1996, 54: 11169–11186
29 Kresse G, Furthmüller J. Efficiency of *ab-initio* total energy calculations for metals and semiconductors using a plane-wave basis set. Comput Mater Sci, 1996, 6: 15–50
30 Blöchl PE. Projector augmented-wave method. Phys Rev B, 1994, 50: 17953–17979
31 Perdew JP, Burke K, Ernzerhof M. Generalized gradient approximation made simple. Phys Rev Lett, 1996, 77: 3865–3868
32 Dudarev SL, Botton GA, Savrasov SY, *et al.* Electron-energy-loss spectra and the structural stability of nickel oxide: An LSDA+U study. Phys Rev B, 1998, 57: 1505–1509
33 Zhang WB, Yu N, Yu WY, *et al.* Stability and magnetism of vacancy in NiO: A GGA+U study. Eur Phys J B, 2008, 64: 153–158
34 Chen W, Wu Y, Fan J, *et al.* Understanding the doping effect on NiO: Toward high-performance inverted perovskite solar cells. Adv Energy Mater, 2018, 8: 1703519
35 Ani MH, Kamarudin MA, Ramlan AH, *et al.* A critical review on the contributions of chemical and physical factors toward the nucleation and growth of large-area graphene. J Mater Sci, 2018, 53: 7095–7111
36 Xia X, Jiang Y, Wan Q, *et al.* Lithium and silver co-doped nickel oxide hole-transporting layer boosting the efficiency and stability of inverted planar perovskite solar cells. ACS Appl Mater Interfaces, 2018, 10: 44501–44510
37 Nukunudompanich M, Budiutama G, Suzuki K, *et al.* Dominant effect of the grain size of the $MAPbI_3$ perovskite controlled by the surface roughness of TiO_2 on the performance of perovskite solar cells. CrystEngComm, 2020, 22: 2718–2727
38 Liu D, Zhou W, Tang H, *et al.* Supersaturation controlled growth of $MAFAPbI_3$ perovskite film for high efficiency solar cells. Sci China Chem, 2018, 61: 1278–1284
39 Wetzelaer GJAH, Scheepers M, Sempere AM, *et al.* Trap-assisted non-radiative recombination in organic-inorganic perovskite solar

cells. Adv Mater, 2015, 27: 1837–1841
40 Chen K, Wu P, Yang W, *et al.* Low-dimensional perovskite interlayer for highly efficient lead-free formamidinium tin iodide perovskite solar cells. Nano Energy, 2018, 49: 411–418
41 Chen W, Wu Y, Yue Y, *et al.* Efficient and stable large-area perovskite solar cells with inorganic charge extraction layers. Science, 2015, 350: 944–948
42 Tan H, Jain A, Voznyy O, *et al.* Efficient and stable solution-processed planar perovskite solar cells *via* contact passivation. Science, 2017, 355: 722–726
43 Jiang Q, Zhang L, Wang H, *et al.* Enhanced electron extraction using SnO_2 for high-efficiency planar-structure $HC(NH_2)_2PbI_3$-based perovskite solar cells. Nat Energy, 2017, 2: 16177
44 Lin HW, Lu CW, Lin LY, *et al.* Pyridine-based electron transporting materials for highly efficient organic solar cells. J Mater Chem A, 2013, 1: 1770–1777
45 Fabregat-Santiago F, Garcia-Belmonte G, Mora-Seró I, *et al.* Characterization of nanostructured hybrid and organic solar cells by impedance spectroscopy. Phys Chem Chem Phys, 2011, 13: 9083–9118
46 Liu C, Wang K, Du P, *et al.* Efficient solution-processed bulk heterojunction perovskite hybrid solar cells. Adv Energy Mater, 2015, 5: 1402024

Acknowledgements The authors greatly thank the Instrument Analysis Center and Electron Microscope Center of ShanghaiTech University. This work was supported by the National Key Research and Development Program of China (2016YFA0204000), the National Natural Science Foundation of China (61935016, U1632118 and 21571129), start-up funding from ShanghaiTech University, Young 1000 Talents Program, Science Fund for Creative Research Groups (21421004), and the Center for High-resolution Electron Microscopy (ChEM) at ShanghaiTech University (EM02161943).

Author contributions Chen H and Ning Z designed and directed this study; Chen H carried out all the experiments; Peng Z, Xu K, Yu D, Han C and Li H helped material and device characterizations; Wei Q carried out and interpreted the DFT caculations; Ning Z supervised the whole project; Chen H wrote the manuscript and Ning Z revised it. All authors discussed the results and commented on the final manuscript.

Conflict of interest The authors declare that they have no conflict of interest.

Supplementary information Experimental details and supporting data are available in the online version of the paper.

Hao Chen is a PhD candidate in materials physics and chemistry, School of Physical Science and Technology, ShanghaiTech University, China. He received his BS degree in chemical engineering and technology from Xiangtan University in 2014. From 2019 to 2020, he is a visiting student in the Department of Electrical and Computer Engineering, University of Toronto. His current research interests include single-junction perovskite solar cells and tandem solar cells.

Zijian Peng is currently a master student at the School of Physical Science and Technology, ShanghaiTech University. He received his BS degree in materials chemistry from Sun Yat-sen University in 2013. His curent research interest mainly focuses on highly efficient and stable perovskite solar cells.

Zhijun Ning is an assistant professor at the School of Physical Science and Technology, ShanghaiTech University, China. He received his PhD degree from the Department of Applied Chemistry, East China University of Science and Technology. From 2011 to 2014, he was a Postdoctoral Scholar in the Department of Electrical and Computer Engineering, University of Toronto. His current research interest focuses on solution-processed optoelectronic materials and devices.

基于能带工程制备氧化镍基底的高效锡-铅共混钙钛矿太阳能电池

陈昊[1,2,3†], 彭子键[1†], 徐凯敏[1], 魏旗[1], 虞丹妮[1], 韩聪聪[1], 李晗升[1], 宁志军[1*]

摘要 钙钛矿叠层太阳能电池因为具有超过肖克利-奎伊瑟效率极限的潜力而备受关注. 窄带隙锡-铅(Sn-Pb)共混钙钛矿太阳能电池(PSCs)在钙钛矿叠层太阳能电池的构建中起着关键作用. 制备稳定性好、可低温处理的空穴输送层是构建高效Sn-Pb钙钛矿太阳能电池和钙钛矿叠层太阳能电池的关键. 在此, 我们开发了一种室温处理的纳米晶体氧化镍(L-NiO_x)作为空穴传输层用于Sn-Pb共混钙钛矿太阳能电池结构. 相比于高温烧结的氧化镍(H-NiO_x)薄膜, L-NiO_x表现出较深的价带和较低的陷阱密度, 这增大了内建电势和减少了载流子的复合, 使器件的功率转换效率达到了18.77%, 这是基于NiO_x空穴传输层的窄带隙Sn-Pb钙钛矿太阳能电池的最高效率. 此外, 该器件的效率在50天后仍能保持原有效率的96%, 具有非常好的稳定性. 这项工作为高效稳定窄带隙PSCs提供了一种可在室温下制备的无机空穴传输材料.